Numerical study on influence of hydrofoil clearance towards total drag reduction on winged air induction pipe for air lubrication

Yanuar[1], Made Susena Griya Putra[1]

ARTICLE INFO

ABSTRACT

A new device for air lubrication called Winged Air Induction Pipe (WAIP) is studied in the present work. The device, which consists of angled hydrofoil uses the low-pressure region produced above the hydrofoil as ship moves forward. The low pressure drives the atmospheric air into the water in certain velocities which the pressure is negative compare to atmospheric pressure. A computational fluid dynamics approach is presented to study the effect of hydrofoil clearance of Winged Air Induction Pipe in drag reduction experienced by the plate which WAIP attached. The well-known 'volume of fluid' model and $\kappa - \omega$ SST (shear stress transport) turbulence closure model have been used in the 2D numerical simulation in ANSYS Fluent. The numerical simulation is carried out with different configuration of hydrofoil clearance and angle of attack. Effects of these parameters on total drag force and drag reduction are reported. The reduction of drag force is found to increase to about 10% compared to bare plate configuration.

1. Introduction

The methods of drag reduction using air lubrication are becoming promising study due to the increase of fuel efficiency produced as the result of reduced drag. The principle of air lubrication method is to reduce the Reynold shear stress occurs on the boundary layer of the flow (Yanuar, et al., 2012). The magnitudes of the Reynold shear stress can be moderately changed by the dispersed phase for the dilute two-phase flow, but the distribution pattern keeps unchanged (Muste, et al., 2009). (Kodama et al.,2000; Takahashi et al., 1995, 2000) found promising result using air lubrication in the form of microbubble for drag reduction. It is well known that the presence of the air in the turbulent boundary layer of the flow leads to drag reduction for two reasons: first by lowering the average viscosity and density of the mixture flow. The mixture of gas and liquid has lower density and viscosity compare to the liquid itself; second, by decreasing the magnitudes of the Reynold shear stress through the interaction of the air and liquid.

Numerical study also can be performed to calculate drag reduction produced by air lubrication. Numerical study has been done as an alternative to experimental study as the numerical requires less time and still gives accurate result by conducting validation towards the similar experimental result first. Various numerical study has been performed to calculate the drag reduction using various air lubrication. (Mohanarangam, et al., 2009) studied the phenomenon of drag reduction by the drag reduction by the injection of microbubble into a turbulent boundary layer using an Eulerian-Eulerian two-fluid model. (Pang, et al., 2014) investigated microbubble drag reduction using the Euler-Lagrange two-way coupling method in order to understand the drag reduction mechanism by microbubbles. (Shereena, et al., 2014) conducted a numerical simulation using $\kappa - \omega$ SST to calculate the drag reduction produced by air jet on an axisymmetric underwater vehicles.

The air lubrication requires an injection to disperse air into the water. The injection requires energy due to the higher pressure in the water particularly in certain depth in the ship bottom hull. The pressure from air compressor is required in order to inject air into the water. However, the amount of energy required is large enough to cancel out a part of the energy saved

[1]Department of Mechanical Engineering, University of Indonesia, Depok, 16424, Indonesia E-mail: made.susena@ui.ac.id

by the air lubrication. The injection of the air into the water in certain depth requires various source of energy: first the adiabatic compression, the air generation in the water and mechanical losses at the air compressor (Kumagai, et al., 2015). As the result, he net-power saving declines as little as 5%. (Kumagai, et al., 2015) found a new device called Winged Air Induction Pipe (WAIP). The WAIP consist of the air pipe and angled hydrofoil that has a lower pressure in the upper surface due to the higher velocity magnitudes. Previously, numerous study on the effect of the hydrofoil on air-water interface has been performed. (Duncan, 1981), conducted and experiment of the breaking waves produces by a towed hydrofoil at constant depth and velocity. (Kumagai, et al., 2011) found that the hydrofoil also produces a negative pressure that pull in the air above into the water as the hydrofoil positioned near the water surface.

In the present work the WAIP from previous work (Kumagai, et al., 2015) is studied. The device produces natural air injection without using an air compressor at critical velocity U_c that is defined as:

$$U_c = \sqrt{\frac{2gH\alpha}{C_P\alpha - (\frac{L}{h_b})C_D\sin\theta}} \qquad (1)$$

where g is gravity acceleration, H is the depth of the injection, α is the mean void fraction, C_P is pressure coefficient, and L, h_b, C_D, and θ are hydrofoil chord length, the air-water mixture layer thickness, and hydrofoil angle of attack respectively. However in their study (Kumagai, et al., 2015) found that the hydrofoil in some cases develop some problem regarding the clearance to the bottom plate where the WAIP placed. Additionally, it should be noticed that the present numerical simulation is aimed to analyze the influence of the hydrofoil clearance in Winged Air Induction Pipe towards the amount of drag reduction produced and the relationship between the angle of attack and clearance of the hydrofoil in WAIP device.

2. Numerical Strategies.

For simulating two phase flow, the Volume of Fluid (VOF), as implemented in Fluent, is used. This can be used to model the separation of air and water above and below the ship respectively. The water is implemented as the primary phase and air as the secondary phase. The surface tension modeling also used in the modeling to achieve representation of the air-water contour.

2.1. Governing Equations.

For simulating turbulent flow, the Shear-Stress Transport (SST) $\kappa - \omega$ is used to model the near wall region of the flow. This is based on previous study that found this model is well suited for simulating two phase flows. (Mohanarangam, et al., 2009). The $\kappa - \omega$ SST model is an effective blend of robust and accurate formulation of the $\kappa - \omega$ in the near wall region and $\kappa - \varepsilon$ model in the far field (Shereena, et al., 2014). The $\kappa - \omega$ SST model gives more realistic result in prediction of void fraction occurs in the near wall region (Menter, 1994). Instead of using empirical wall function to correlate the near wall and far

field region, $\kappa - \omega$ SST solved two turbulence scalar directly towards the wall boundary (Mohanarangam, et al., 2009). SST $\kappa - \omega$ can be described as:

a. Kinematic eddy viscosity

$$\nu_T = \frac{a_1 k}{\max(a_1\omega, S F_2)} \qquad (2)$$

b. Turbulent kinetic energy

$$\frac{\partial k}{\partial t} + U_j\frac{\partial k}{\partial x_j} = P_k - \beta^* k\omega + \frac{\partial}{\partial x_j}\left[(\nu + \sigma_k\nu_T)\frac{\partial k}{\partial x_j}\right] \qquad (3)$$

c. Dissipation rate

$$\frac{\partial\omega}{\partial t} + U_j\frac{\partial\omega}{\partial x_j} = \alpha S^2 - \beta\omega^2 + \frac{\partial}{\partial x_j}\left[(\nu + \sigma_\omega\nu_T)\frac{\partial\omega}{\partial x_j}\right] + 2(1 - F_1)\sigma_{\omega 2}\frac{1}{\omega}\frac{\partial k}{\partial x_i}\frac{\partial\omega}{\partial x_i} \qquad (4)$$

As soon as the air introduced into the water, the flow becomes two phase. The Volume of Fluid is implemented in Fluent. This can be used to model two phase flow and gives representation of the air water interface. the continuity equation of the air-water mixture can be defined as:

$$\frac{\partial\rho_m}{\partial t} + \rho_m\vec{v}_m = 0 \qquad (5)$$

where ρ_m id the density of the mixture, t is time and $\vec{v}_m$ is system average velocity. The formulation of the density and system average velocity can be given as:

$$\rho_m = \sum_{k=1}^{n}\alpha_k\rho_k \qquad (6)$$

$$\vec{v}_m = \frac{\sum_{k=1}^{n}\alpha_k\rho_k\vec{v}_k}{\rho_m} \qquad (7)$$

where α_k is the volume fraction from the k phase, ρ_k is the density of the k phase, and $\vec{v}_k$ if the k phase average velocity. The momentum equation of the air-water mixture can be obtained by summing the individual momentum from each phase. The equation given as:

$$\frac{\partial}{\partial t}\left(\rho_m\vec{v}_m\right) + \nabla.\left(\rho_m\vec{v}_m.\vec{v}_m\right) = \nabla p + \nabla.\left[\mu_m\left(\nabla\vec{v}_m + \nabla\vec{v}_m^T\vec{v}_m^T\right)\right] + \rho_m g + \vec{F} + \nabla.\left(\sum_{k=1}^{n}\alpha_k\rho_k\vec{v}_{dr,k}\vec{v}_{dr,k}\right) \qquad (8)$$

p is pressure, g is the gravity acceleration, $\vec{F}$ is the body force intensity, and μ_m is air-water mixture dynamic viscosity that can be expressed as:

$$\mu_m = \sum_{k=1}^{n}\alpha_k\mu_k \qquad (9)$$

$\vec{v}_{dr,k}$ is the drift velocity for secondary phase k, defined as:

$$\vec{v}_{dr,k} = \vec{v}_k - \vec{v}_m \qquad (10)$$

where μ_k is the dynamic viscosity of the k phase. The relative velocity is defined as the velocity of a secondary phase p relative to the velocity of the primary phase q.

$$\vec{v}_{pq} = \vec{v}_p - \vec{v}_q \qquad (11)$$

the mass fraction of any phase k given as:

$$c_k = \frac{\alpha_k \rho_k}{\rho_m} \tag{12}$$

drift velocity and relative velocity $\overrightarrow{v}_{pq}$ connected by:

$$\overrightarrow{v}_{dr,p} = \overrightarrow{v}_{pq} - \sum_{k=1}^{n} c_k \overrightarrow{v}_{qk} \tag{13}$$

From the previous continuity equation for secondary phase p, the volume fraction of the secondary phase p can be obtained as:
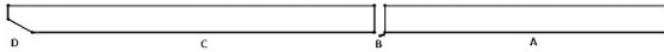
$$\frac{\partial}{\partial t}\left(\alpha_p \rho_p\right) + \nabla \cdot \left(\alpha_p \rho_p v_m\right) = -\nabla \cdot \left(\alpha_p \rho_p \overrightarrow{v}_{dr,p}\right) + \sum_{k=1}^{n}\left(\dot{m}_{qp} - \dot{m}_{pq}\right) \tag{14}$$

where $\dot{m}_{qp}$ and $\dot{m}_{pq}$ is the mass flow rates.
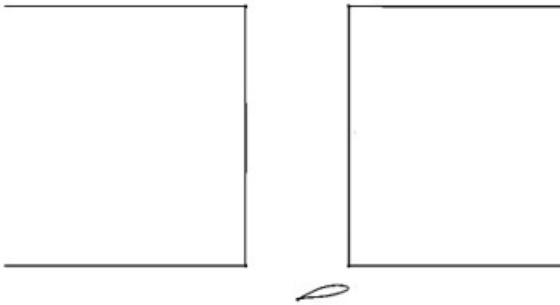
2.2. Computational Domain.

The analyze object is simplified by dividing the model into four parts. As described in the Fig. 2, part A (2,216 mm) is the bare plate, part B (80 mm) is the WAIP, part C (2,600 mm) is bare flat plate that received the effect of the WAIP, and part D (184 mm) is the afterbody.

Figure 1: Schematic diagram from side-view of the computational setup.
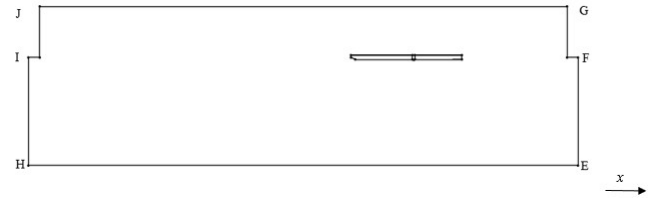

Source: Authors.

Figure 2: Part B: WAIP Setup.

Source: Authors.

The computational domain uses two different in length of plane to separate the air and water. As the segment EFHI is the water boundary and segment FGIJ is the air boundary. The air is treated with 0 velocity and the water is a moving fluid with the velocity of $U_c = 5.6$ m/s (Kumagai, et al., 2015). The details of the boundary conditions are adopted from previous simulation (Shereena, et al., 2014) The boundary condition are: (a) segment EF is a velocity inlet, i.e. where U is pre-described in the −x direction; (b) segment DE is pressure outlet. The rest of the computational domain edges are treated as nonslip wall.
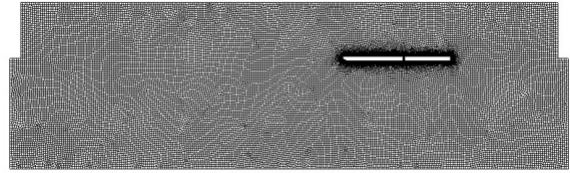
Figure 3: Computational Domain.

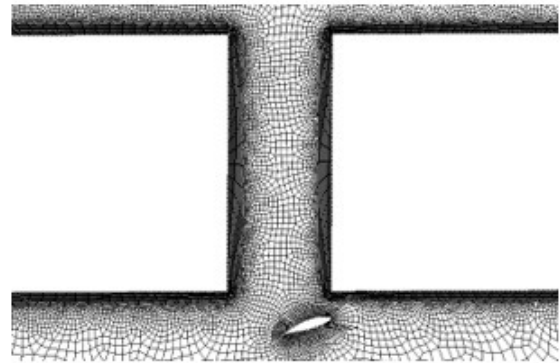Source: Authors.

2.3. Grid and discretization.

A sample of mesh model for the setup is shown in fig. 4. Quadrilateral is applied for the meshing method as it gives more even separation for the air-water interface of the domain. The value for the mesh is done by trial and error to give the most appropriate mesh model for the model. Because the mesh should be evenly distributed around the model. Hence, edge sizing and edge first layer thickness inflation also implemented in the model to give narrower and more even grid distribution towards the surface of the 2D-model.

Figure 4: Mesh Model (No. of Nodes = 201775; No. of elements = 196401).

Source: Authors.

Figure 5: Enlarged view of mesh for part B (clearance = 20mm; angle of attack = 20º).

Source: Authors.

The volume fraction of air is given as 1 for the segment FGIJ, and 0 for the segment EFHI. In this work, second order upwind scheme is used in all calculation using a pressure based computation. All numerical simulation is done using transient solution. The convergence criterion for numerical parameters are all set to 10^{-3} for velocity, continuity, k, and ω The time step used in simulation is 0.001s with number of time steps of 20 and 20 iterations.

Figure 6: Two dimensional representation of air-water interface on computational domain.

Source: Authors.

3. Validation.

(Kumagai, et al., 2015) conducted and experimental study in the drag reduction measurement produced by the WAIP in part C. The result shows the magnitude of drag experienced by part C for each configuration of the WAIP. The bare plate configuration also presented for the purpose of calculation of drag reduction, where Db is the drag of the part C.

Table 1: Experimental data.

Experimental Data with 15 mm of Clearance (Kumagai, et al., 2015)					
Type	θ°	v (m/s)	Db (N)	ΔD_b (N)	DR (\%)
Bare Plate	Bare	5.6	181.49	-	-
WAIP	12	5.6	167.75	-13.73	7.57
WAIP	16	5.6	166.77	-14.72	8.11
WAIP	20	5.6	162.85	-18.64	10.27

Source: Authors.

The numerical simulation of the same geometry is adopted and similar simulations were performed for the validation purposes.

Table 2: Numerical data.

Numerical Data					
Type	θ°	v (m/s)	Db (N)	ΔD_b (N)	ΔR (\%)	Error
Bare Plate	Bare	5.6	173.48	-	-	4.41\%
WAIP	12	5.6	155.24	-18.24	10.51	7.46\%
WAIP	16	5.6	156.63	-16.86	9.72	6.08\%
WAIP	20	5.6	177.53	4.05	-2.33	9.02\%
Error						6.74\%

Source: Authors.

Since some of vital data such as plate draught, and the length of afterbody were not reported in the paper, the validation is somewhat approximate and shows error of 6.74%. From the result obtained, it is concluded that Volume of Fluid model and k-ω SST turbulence model are the appropriate computational model for this case of problem.

4. Result and Discussion

The drag on the part C is showed in table 3, 4, and 5 for each configuration of clearance of 10 mm, 15 mm, 20 mm respectively, and angle of attack of the hydrofoil of 12∘, 16∘, and 20∘, where F_p, F_v, F_t, C_p are pressure drag, viscous drag, total drag, and coefficient of pressure respectively.

Table 3: Pressure and viscous drag of part C (clearance = 10 mm; Re = 1.49×10^7).

Clearance 10 mm						
θ°	U (m/s)	Fp	Fv	Ft	Cp	Fv'	Ft'
12	5.60	0	97.03	97.03	0	158.41	158.41
16	5.60	0	97.64	97.64	0	159.42	159.42
20	5.60	0	96.80	96.80	0	158.04	158.04

Source: Authors.

Table 4: Pressure and viscous drag of part C (clearance = 15 mm; Re = 1.49×10^7).

Clearance 15 mm						
θ°	U (m/s)	Fp	Fv	Ft	Cp	Fv'	Ft'
12	5.60	0	95.09	95.09	0	155.24	155.24
16	5.60	0	95.93	95.93	0	156.63	156.63
20	5.60	0	108.74	108.74	0	177.53	177.53

Source: Authors.

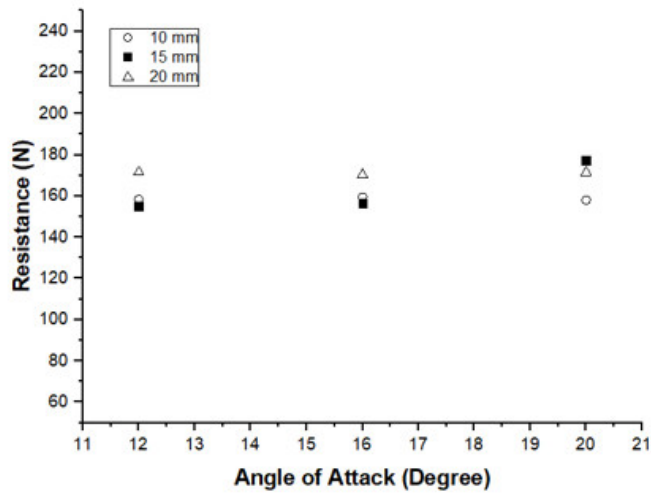Table 5: Pressure and viscous drag of part C (clearance = 20 mm; Re = 1.49×10^7).

Clearance 20 mm						
θ°	U (m/s)	Fp	Fv	Ft	Cp	Fv'	Ft'
12	5.60	0	105.11	105.11	0	171.61	171.61
16	5.60	0	104.37	104.37	0	170.40	170.40
20	5.60	0	105.03	105.03	0	171.48	171.48

Source: Authors.

A visualization of total drag experienced by part C is shown in fig. 7 for each clearance of 10 mm, 15 mm, and 20 mm respectively.

The simulation is conducted without performing air injection from the hull pipe in the WAIP device to proof the critical velocity in (1) could produce the phenomenon of air entrainment due to the negative pressure produced by the hydrofoil. The critical velocity of 5.6 m/s is used in the simulation according to previous experiment (Kumagai, et al., 2010). The result of total drag from part C shows the distribution of the obtained data has no particular tendency. On the clearance of 10 mm, the smallest value of total drag is obtained in the angle of attack of 20º which has a very small difference in value compares to the 12º, and reach the maximum value at 16º. Otherwise, on the clearance of 20 mm, the minimum value is obtained at

Figure 7: Total drag experienced by part C.

Source: Authors.

16º. However, on the clearance of 15 mm, the magnitude of total drag increased drastically. This phenomenon caused by the flow of the fluid that occurs due to the presence of hydrofoil. The fluid flow occurs on the downstream side of the hydrofoil is difficult to be mapped as a function. Hydrofoil always has a tendency to experienced larger value of drag as the angle of attack increased (Ockfen & Matveev, 2009). However, in this case study is performed to analyze the effect produced by the hydrofoil towards the total drag experienced on part C, the results could not explain explicitly whether the data has a tendency towards particular trends. A large number of variation of angle of attack is needed to really find the exact plot of the phenomena. In the previous work (Kumagai, et al., 2011) also said that the fundamental flow physics concerning this facility has not been clarified yet because extremely complicated phenomena, which are the free-surface effect of the hydrofoil. However, from the result above it is can be obtained that the 10 mm clearance gives the smallest value of mean total drag.

The zero value of the pressure drag of the part C is due to the flow stream does not cross the plate, instead the flow is parallel to the plate. Thus the plate only experienced viscous drag due to the viscosity of the fluid.

On the WAIP (part B), the total drag is obtained by summing the pressure drag and viscous drag experienced by the hydrofoil. The drag component of each clearance of 10 mm, 15 mm, and 20 mm respectively is shown in table 6, 7 and 8.

Table 6: Pressure and viscous drag of part C (clearance = 10 mm; Re = 1.49×10^7).

		Clearance 10 mm				
$\theta°$	U (m/s)	Fp	Fv	Ft	Cp	Fv'	Ft'
12	5.60	49.13	3.41	52.54	80.22	5.57	85.79
16	5.60	74.85	3.18	78.04	122.21	5.19	127.41
20	5.60	91.41	2.60	94.01	149.24	4.25	153.49

Source: Authors.

Table 7: Pressure and viscous drag of part C (clearance = 15 mm; Re = 1.49×10^7).

		Clearance 15 mm				
$\theta°$	U (m/s)	Fp	Fv	Ft	Cp	Fv'	Ft'
12	5.60	43.33	3.31	46.64	70.74	5.41	76.15
16	5.60	71.48	3.36	74.83	116.70	5.48	122.18
20	5.60	192.79	1.82	194.61	314.75	2.97	317.73

Source: Authors.

Table 8: Pressure and viscous drag of part C (clearance = 20 mm; Re = 1.49×10^7).

		Clearance 20 mm				
$\theta°$	U (m/s)	Fp	Fv	Ft	Cp	Fv'	Ft'
12	5.60	78.66	2.64	81.30	128.42	4.31	132.73
16	5.60	133.53	2.04	135.57	218.01	3.32	221.34
20	5.60	195.03	1.59	196.62	318.41	2.60	321.01

Source: Authors.

The hydrofoil experienced pressure drag due to its surface intersecting the fluid's streamline. Thus, the molecule impacts the surface of the hydrofoil and resulting non-zero value of pressure drag. The visualization of the influence of clearance and angle of attack on pressure coefficient of the hydrofoil is shown in fig. 8.
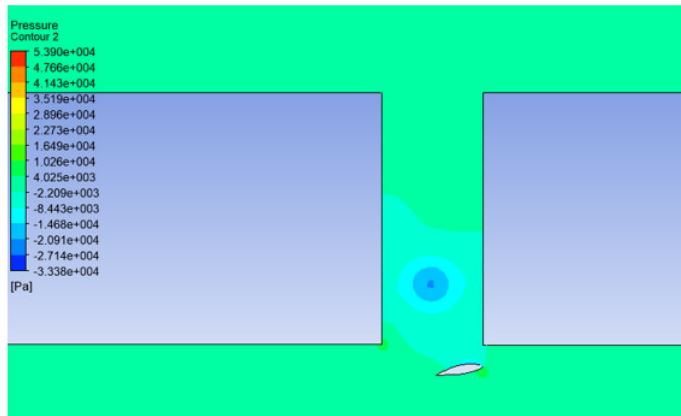
Figure 8: Pressure coefficient of the hydrofoil.

Source: Authors.

As can be seen on fig. 8, the pressure coefficient of the hydrofoil has a tendency to increase as the angle of attack increase. As theoretically expected, the drag force increase as the angle of attack is increased (Ockfen & Matveev, 2009). The increased of angle of attack resulting in increase of angle from intersection line between the hydrofoil's chord line and the fluid's streamline. As a result, a larger amount of energy to deflect the

Figure 9: Contour of dynamic pressure on part B.

Source: Authors.

stream is required. The energy is obtained from kinetic energy which in this case is the moving fluid. On the actual condition, the model is moving through the water resulting the kinetic energy is produced by the object instead of the fluid. Thus, the energy loss is experienced by the model. However, since the study is to analyze the drag experienced by part C, further analysis of the hydrofoil's drag is not performed.

A contour plot of dynamic pressure around part B is shown in fig. 9. As can be seen the pressure gets lower in the hull pipe above the hydrofoil. The phenomenon is called the negative pressure, which the pressure is lower compares to its surrounding. The negative pressure is produced as the fluid moves towards the model. The hydrofoil produces lower pressure on its upper surface due to higher velocity caused by longer curvature.

Table 9 shows the magnitude of drag reduction experienced by part C for each configuration of the model, where D_o, is the hydrofoil total drag.
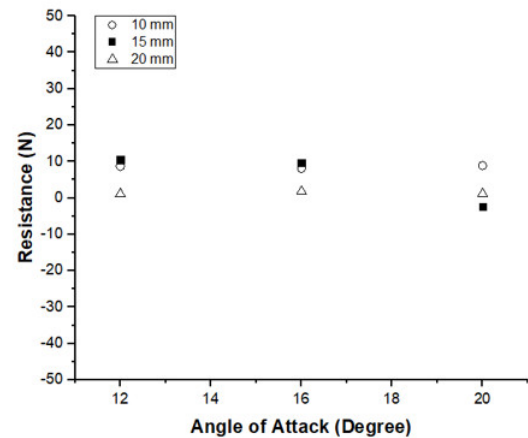
Table 9: Numerical result of influence of hydrofoil clearance on drag reduction of part C.

Clearance (mm)	$\theta°$	U (m/s)	Do	Db	Dt	ΔDo	ΔDb	DR (\%)
-	bare	5.60	174.76	173.48	348.24	-	-	-
10	12	5.60	85.79	158.41	244.20	-88.98	-15.07	8.69
	16	5.60	127.41	159.42	286.82	-47.35	-14.06	8.11
	20	5.60	153.49	158.04	311.54	-21.27	-15.44	8.90
15	12	5.60	76.15	155.24	231.39	-98.62	-18.24	10.51
	16	5.60	122.18	156.63	278.80	-52.58	-16.86	9.72
	20	5.60	465.42	177.53	642.95	290.66	4.05	-2.33
20	12	5.60	132.73	171.61	304.34	-42.03	-1.88	1.08
	16	5.60	221.34	170.40	391.74	46.58	-3.08	1.78
	20	5.60	321.01	171.48	492.49	146.25	-2.00	1.15

Source: Authors.

Table 9 shows the value of the drag reduction for each configuration of the model. The clearance of the hydrofoil gives a significant influence for the drag reduction. However, the value of the drag reduction has no particular tendency towards certain point. Therefore, the appropriate design is obtained by using trial and error method. This is due to the unique flow characteristic produce by the hydrofoil interacts with the plate in part

Figure 10: Drag reduction of part C.

Source: Authors.

C in different ways depend on the clearance between hydrofoil and the bottom plate of the model. On the clearance of 10 mm 8-9\% of drag reduction is obtained. However, on the clearance of 15 mm, there is an added drag of 2\% on angle of attack of 20°. In this case the data is referred as outlier or data that is outside the trend line (Mittink, et al., 2001). Outlier is a common data in data distribution that is not follow the normal distribution. This can be caused by error from numerical computation that has been performed where the mesh element relatively, is not evenly distributed. As a result, the computational result has a large value of error. The distribution of mesh is depended on the element size of the mesh. The element size has to be adjusted to fit the model set up regarding the distance between two or more surface/edge of the model. Generally, as the element of the mesh get smaller the more accurate the result gathered. However, this is could not be corresponded that the finest possible gives the best result. Thus the grid independency test has to be performed in future work. But as the error of the numerical data is less than 10 percent the result obtained is somewhat approximate regarding to the validation performed. In some modeling, to reach solution's grid independency, numerical value in the computational domain (the sizing parameter of mesh element) should be much smaller than corresponding local value of the model so that the numerical error could be minimized (Wang & Zhai, 2012).

Conclusion

Computational Fluid Dynamics approach to estimate the drag reduction by air lubrication using Winged Air Induction Pipe (WAIP) is performed in the present study and reasonably validated with experimental works. By using nine configurations to achieve the effect of hydrofoil clearance towards the drag reduction it is concluded that: the magnitude of drag reduction can be achieved when the contributing parameter which are the angle of attack and hydrofoil clearance chose at their optimum range. The optimum range is achieved by modification of the parameter using trial and error method. The modification

of hydrofoil clearance of the WAIP does not give a data trend to a certain way. The application of WAIP gives result of net drag reduction up to 10\%.

References

Cui, Z., Fan, J. M. \& Park, A.-H., 2003. Drag coefficient for a settling sphere with microbubble drag reduction effects. Powder Technology, pp. 132-134.

Duncan, J., 1981. An Experimental Investigation of Breaking Waves Produced by a Towed Hydrofoil. Proceedings of the International Society of London. Series A, Mathematical and Physical Science, Vol. 377, No. 1779, pp. 331-348.

Evans, G., Jameson, G. \& Atkison, B., 1992. Prediction of the Bubble Size Generated bu a Plunging Liquid Jet Bubble Column. Chemical Engineering Science, Volume 47, pp. 3265-3272.

ITTC, 2011. Recomended Procedures and Guidelines : Practical Guidelines for Ship CFD Application. Kansas: ITTC.

Kodama, Y., Kakugawa, A., Takahashi, T. \& Kawashima, H., 2000. Experimental study on microbubbles and their applicability to ships. Heat and Fluid FLow, pp. 1-7.

Kumagai, I. et al., 2011. Flow behavior around a hydrofoil close to a free surface. Visualization of Mechanical Processes 1 *(3)*.

Kumagai, I. et al., 2010. A new power-saving device for air bubble generation: hydrofoil air pump for ship drag reduction. Proceedings of the International Conference on Ship Drag Reduction (SMOOTH-SHIP), pp. 93-102.

Kumagai, I., Takahashi, Y. \& Murai, Y., 2015. Power-saving device for air bubble generation using a hydrofoil to reduce ship drag: Theory, experiments, and application to ship. Ocean Engineering, pp. 183-195.

Menter, F., 1994. Zonal Two Equation Eddy Viscosity Turbulence Model for Engineering Applications. AIAA Journal, Volume 32, pp. 1598-1605.

Mittink, S., S.T., R. \& Samorodnitsky, G., 2001. The Distribution of Test Statictic for Outlier Detection in Heavy-Tailed Samples. Mathematical and COmputer Modeling, Volume 34, pp. 1171-1183.

Mohanarangam, K., Cheung, S., Tu, J. \& Chen, L., 2009. Numerical simulation of microbubble drag reduction using population balance model. Ocean Engineering, Volume 36, pp. 863-872.

Munson, B. R., Young, D. F., Okiishi, T. H. \& Huebsch, W. W., 2009. Fundamentals of Fluid Mechanics. West Virginia: John Willey and Sons.

Muratoglu, A. \& Yuce, M. I., 2015. Performance Analysis of Hydrokinetic Turbine Blade Sections. Advances in Renewable Energy, Volume 2, pp. 1-11.

Muste, M., Yu, K., Fujita, I. \& Ettema, R., 2009. Two-phase flow insights into open-channel flows with suspended particles of different densities. Environ Fluid Mech, pp. 161-186.

National Research Council, 2007. Assessment of Wingtip Modification to Increase the Fuel Efficiency of Air Force Aircraft. 10 penyunt. Washington: National Academy of Sciences.

Ockfen, A. E. \& Matveev, K. I., 2009. Aerodynamics characteristic of NACA 4412 airfoil section with flap in extreme ground effect. International Journal of Naval Architeture and Ocean Engineering , 1(2013), pp. 1-12.

Pang, M., Wei, J. \& Yu, B., 2014. Numerical Study on modulation of microbuble on turbulence frictional drag in a horizontal channel. Ocean Engineering, Volume 81, pp. 58-68.

Shereena, S., S., V., V.G., I. \& Bhattacharyya, 2014. CFD Study of Drag Reduction in Axissymetric Underwater Vehicles using Air Jets. Engineering Application of Computational Fluid Mechanics, Volume 7, pp. 193-209.

Toffoli, A., Babanin, A., Onorato, M. \& Waseda, T., 2010. Maximum steepness of oceanic waves: Field and laboratory experiments. Geophysics Research Letters, Volume 37.

Wang, H. \& Zhai, Z. (., 2012. Analyzing grid independency and numerical viscosity of computational fluid. Building and Environment, Volume 52, pp. 107-118.

Yanuar, Ibadurrahman, Karim, S. \& Ichsan, M., 2017. Experimental study of the interference resistance of pentamaran asymmetric side-hull. AIP Conference Proceedings. doi: 10.10-07/s11804-012-1136-z